Constraining Magma Ascent Rate Using Water Diffusion in Olivine and Clinopyroxene — Mt Pavlof, Alaska

Nicholas Culbreth

April 28th, 2020

Dr. Megan Newcombe

GEOL394

Abstract

Magma ascent and eruptive style are dominantly controlled by the presence and behavior of dissolved volatiles within the magma. Volatile solubility is in turn controlled by pressure, and to a lesser degree temperature, melt composition, and volatile speciation (e.g. H_2O, OH, CO_2, S). Glassy melt inclusions (MIs) formed during syneruptive crystal growth can trap dissolved volatiles, providing snapshots of the physical and chemical conditions present during magma ascent. Magma degasses dissolved volatiles as pressure decreases during ascent, creating a concentration gradient of volatiles in crystals. Comparison between initial volatile concentrations, as preserved in MIs, and observed water concentration gradients in rapidly quenched crystals allows the constraint of magma ascent rate. FTIR analysis of three melt inclusions hosted in olivine phenocrysts from the 2016 eruption of Mount Pavlof, Alaska shows a range of 1.13 to 2.5 wt% H_2O. Compositional constraints were placed on the grains using rhyolite-MELTs, a thermodynamics-driven phase equilibrium software. VolatileCalc 2.0, a software package for calculating volatile solubility in magma, was used to construct a magma-degassing path for the 2016 eruption based on the melt inclusion with the highest water concentration. Modeling of diffusive water loss in a clinopyroxene grain from the 2016 eruption using the inclusion-derived degassing path yields a syneruptive magma ascent rate of 0.097 MPa/s. This represents a rapid ascent rate for what has been classified as a mild 2 on the volcanic explosivity index (VEI) — a logarithmic scale of relative eruption intensity.

Table of Contents

1. Introduction

At approximately midnight UTC on March 28th, 2016, Mount Pavlof, Alaska, erupted abruptly, without any detectable seismic precursors. Over the next 29 hours Mt. Pavlof emitted an ash plume up to 9 km in height that would extend over 600 km to the northeast — resulting in the cancelation of over 100 flights in Alaska and northwestern Canada (Fee et al., 2017). This eruption marks the most recent addition to a list of more than 40 eruptions recorded at Mt. Pavlof over the last 200 years. Mt. Pavlof's location along major intercontinental flightpaths and its status as the Aleutian Arc's most active volcano makes it a significant ongoing hazard (Mangan et al., 2009).

Mt. Pavlof presents an ideal location to investigate eruptive processes. Its frequent eruptions vary widely, covering a range of styles including Hawaiian fire fountain, effusive Strombolian, and explosive Plinian and sub Plinian eruptions (Larsen, 2016). Mt. Pavlof is particularly suited to diffusion modeling, where an "open vent" conduit discourages stalling of magma during ascent that could otherwise reset diffusion clocks (Mangan et al., 2009). For these reasons, we seek to constrain the syneruptive magma ascent rate of the 2016 eruption and explore the relationship between ascent rate, eruptive style, and intensity.

2. Background

2.1 Volcanic Explosivity Index

Volcanic eruptions display a great range of eruptive style, power, and duration. This diversity can be observed between different volcanic systems as well as in temporally separated eruptions within individual volcanoes. Historically, this variance in eruptive characteristics has been a significant hindrance in quantitative comparisons of eruptions (Newhall and Self, 1982). To unify previous attempts at classifying eruptive magnitude, Newhall and Self (1982) developed the now ubiquitous volcanic explosivity index (VEI).

Much like Richter magnitude for earthquakes, the VEI offers a logarithmic scale for classifying the explosive character of an eruption. The VEI scale ranges from 0 to 8 (Fig. 1) and is a foremost a measurement of total of erupted material volume, with a VEI of 1 representing ejecta volumes of 10^4 to 10^6 m^3. Eruptions with less than 10^4 m^3 of ejecta are classified as a VEI of 0. Eruptions between 10^6 and 10^7 m^3 are classified as VEI 2, after which the scale continues increasing logarithmically. Additional considerations are made for ejecta column height, ejecta production rate, and duration. Considering an assemblage of eruptive characteristics allows the classification of historic eruptions where data may be incomplete (Newhall and Self, 1982).

2.2 Volatile Controls on Eruptive Style

Broadly speaking, volcanic eruptions can be divided into effusive or explosive eruptions. Explosive eruptions can be further divided into those that interact with external water sources and those that don't. Eruptions belonging to the latter group, including those recorded at Mt. Pavlof, are referred to as "dry". Dry eruptions are primarily controlled by the speciation and concentration of magmatic volatiles (largely H_2O and CO_2), magma rheology, and eruption rate (Gonnerman and Manga, 2012).

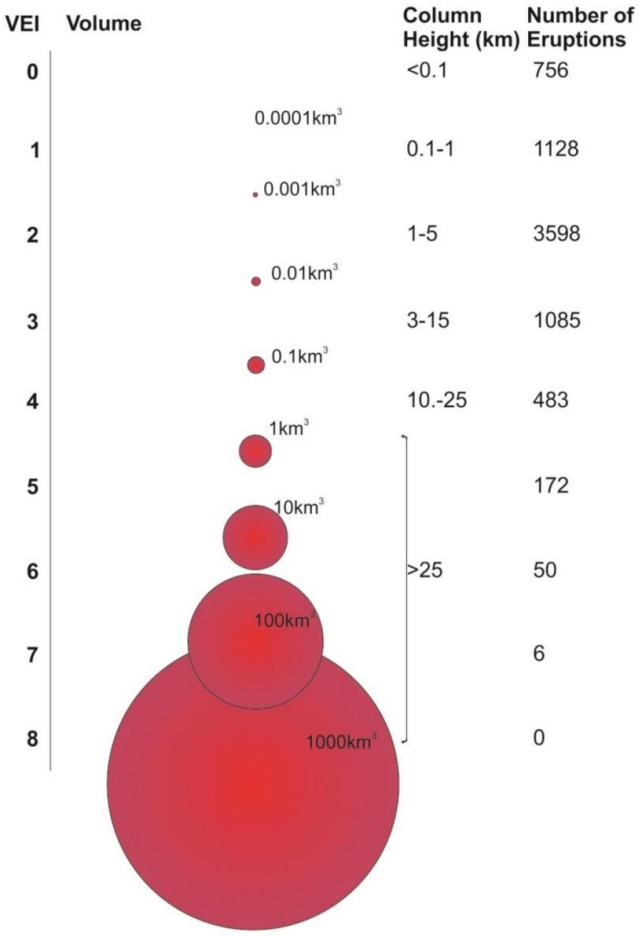

Fig. 1: Graphic representation of VEI scale displaying ejecta volume, column height, and number of confirmed Holocene eruptions at each VEI. From Loughlin et al., 2015.

Prior to eruption, magma is stored at depth in magma chambers. Magma chambers can become over pressurized by tectonic forces, magma replenishment, and/or the exsolution of volatiles during crystallization. Magma ascent initiates when the chamber pressure exceeds the frictional and magma-static forces containing the magma. Volatiles, particularly water, control the ascent of magma through the conduit. Dissolved volatiles influence magma viscosity, while exsolved volatiles exert multiple controls on the ascent process (Gonnerman and Manga, 2012).

Volatile solubility is primarily a function of pressure, resulting in the supersaturation of volatiles if ascent is faster than the diffusion of volatiles into existing bubbles (Toramaru, 1989). Supersaturation accelerates the nucleation of exsolved volatile bubble nucleation, which increases magma buoyancy and promotes crystallization. Fractional crystallization further concentrates volatiles within the remaining melt, resulting in a feedback loop. At a critical bubble volume fraction the magma fragments, converting what was a bubbly magma flow into an explosive gas flow containing magma fragments (Zhang et al., 2007). The fragmentation of magma leads to the explosive ejection of pyroclasts from the

volcanic vent (Fig. 2). The size and volume of ejected pyroclasts is determined by the type and efficiency of fragmentation (Gonnermann and Manga, 2012).

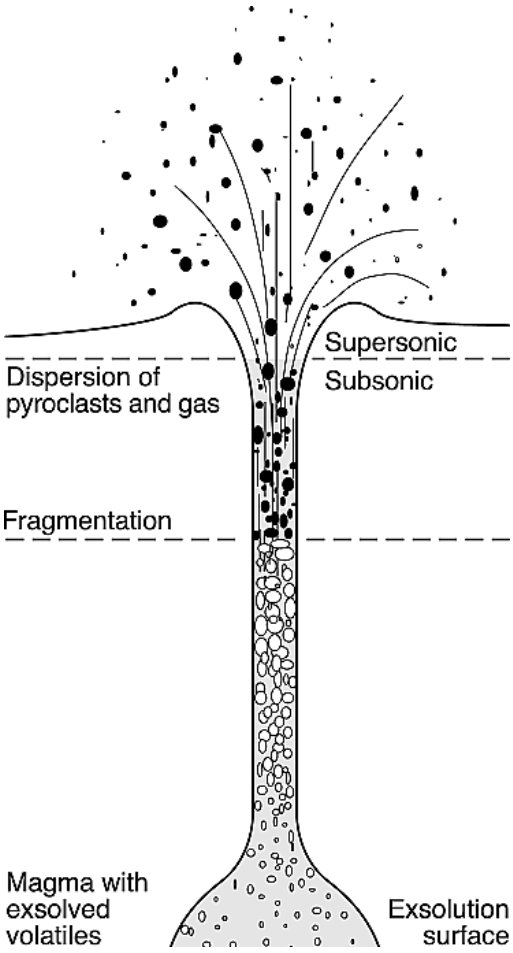

Fig. 2: Stages of an explosive eruption. Bubble nucleation begins at the exsolution surface. Fragmentation occurs when exsolved bubbles break and release trapped gas. From Zhang et al., 2007.

2.3 Water Diffusion in Olivine and Clinopyroxene

Olivine and clinopyroxene are nominally anhydrous minerals (NAMs) yet can incorporate trace amounts of water in structural defects. This water takes the form of H^+ ions associated with cation vacancies ($2H^+$ vs Mg^{2+}) or OH^- associated with charge deficiencies (Al^{3+} vs Si^{4+}) (Weis et al., 2018). Water concentrations within NAMs are dependent on the concentration of dissolved water within the host magma. Magma water solubility is primarily a function of pressure, with ascending magma degassing and losing its dissolved water to bubbles. NAMs continuously equilibrate with the degassing magma, resulting in diffusive water loss over time. MIs within NAMs undergo water loss by diffusion of H^+ through the host NAM based on the diffusivity of water in the NAM, the partition coefficient between the melt and NAM, the size of the MI, and the distance between the MI and NAM rim (Chen et al., 2013). However, magmas can ascend faster than MIs are capable of equilibrating with the melt through H^+ diffusion. Under these circumstances, MI water concentrations are reflective of the magma at the time they were captured.

Prior researchers have determined water diffusion rates in olivine and clinopyroxene by analog experiments performed on natural and synthetic grains of olivine and clinopyroxene polished into rectangular prisms and cubes. These experiments have shown orders of magnitude differences in diffusion rates based on composition and crystallographic orientation (Woods et al., 2000; Ferriss et al., 2016; Lloyd et al., 2016; Ferriss et al., 2018). Experimentally derived diffusion rates and initial water concentrations, as measured in MIs, can be used to model time dependent diffusion gradients. Measured diffusion gradients in NAMs hosting MIs can be compared with time dependent models to constrain the ascent rate of the observed NAM (Fig. 3) (Barth et al., 2019).

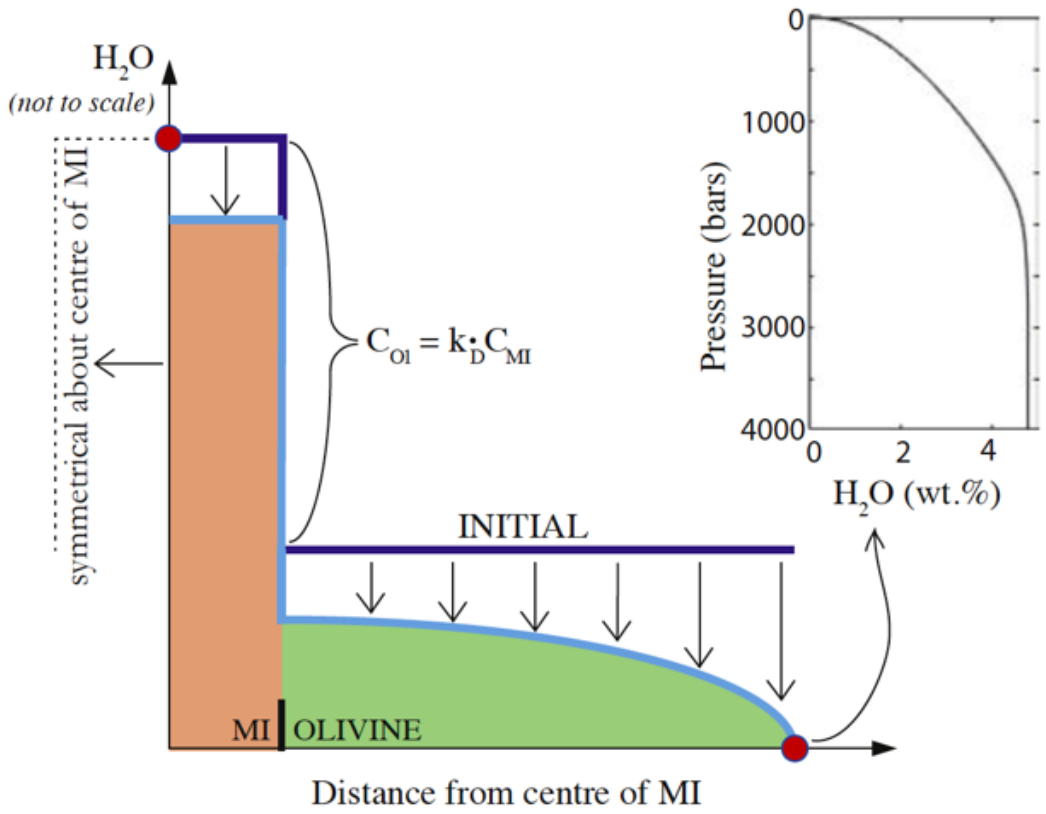

Fig. 3: Diffusive water loss across an olivine grain. The initial water concentration of the olivine is the product of the melt inclusion's water concentration (C_{MI}) and the partition coefficient of water between the inclusion and olivine (K_D). Syneruptive diffusive loss of the initial olivine water content results in a decrease in measured water concentration towards the crystal rim. Adapted from Barth et al., 2019.

3. Objectives

The goal of this research is to constrain the magma ascent rate of Mount Pavlof's 2016 eruption by measuring water concentrations in olivine MIs and water diffusion in clinopyroxene using Fourier-transform infrared spectroscopy. The hypothesis is that the magma ascent rate of the 2016 Mt. Pavlof eruption falls outside the uncertainty of ascent rates for comparable VEI 2-3 eruptions, as evidenced by the eruption's large plume height. The null hypothesis is that the magma ascent rate is within the uncertainty of comparable VEI 2-3 eruptions.

Quantifying the magma ascent rate at Mt. Pavlof offers new insights into the magmatic processes of Mt. Pavlof and the greater Aleutian volcanic arc. Prior research indicates that ascent rate is the primary control of mass eruption rate (Fig. 4) (Barth et al., 2019) — which, in combination with magma viscosity, controls eruptive style (Gonnerman and Manga, 2012). Validation, or invalidation, of the current understanding of the relationship between ascent rate and eruptive style has implications for hazard management within and beyond the Mount Pavlof volcanic system.

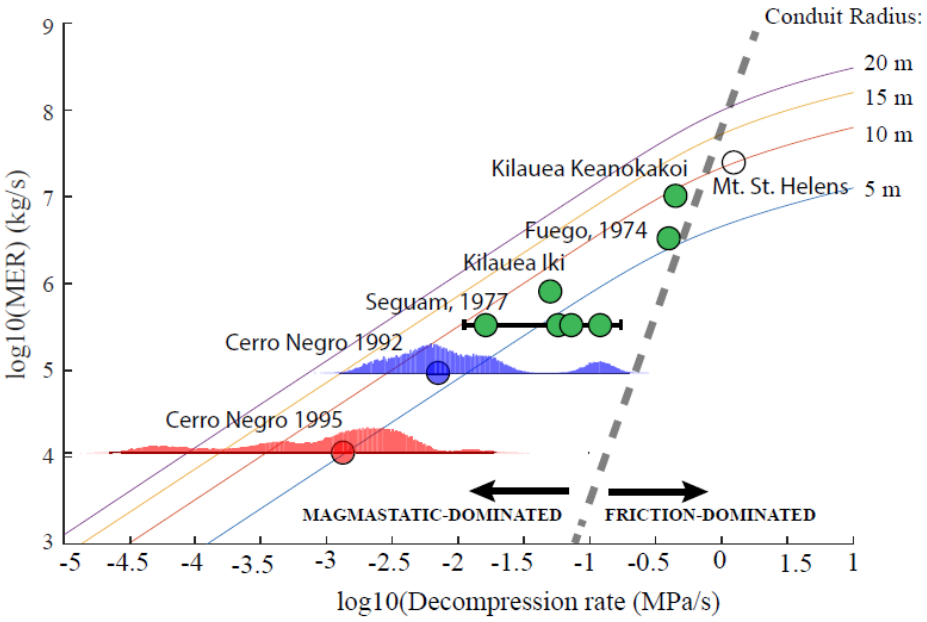

Fig. 4: Mass eruption rate vs. decompression rate. Solid lines indicate solutions to conduit flow models assuming a constant conduit radius and ascent rate. Fee et al., 2017 proposes a syneruptive conduit radius of ~10 m for Mt. Pavlof. Adapted from Barth et al., 2019.

4. Methods

4.1 Sample Preparation

The Alaskan Volcano Observatory collected erupted material from Mt. Pavlof in the weeks following the 2016 eruption. Tephra samples were collected from ashfalls on fresh snowbanks to prevent contamination from previous eruptions. The sample PAV-AT3742 has been provided by the Alaskan Volcano Observatory. The sample was sieved to isolate grains between 250 and 1000 microns. The isolated grains were mass separated using heavy liquids by Dr. Megan Newcombe; mafic phases with densities greater than 2.85 g/cm^3, specifically olivine and clinopyroxene, were isolated. The nominally anhydrous nature and early crystallization of olivine and clinopyroxene make them ideal for water diffusion analysis.

A Leica S9i transmitted light microscope was used to identify grains with euhedral habit and large melt inclusions (Fig. 5). Three olivine phenocrysts hosting melt inclusions and one inclusion-free clinopyroxene phenocryst were selected for further analysis. The

selected grains were set in Crystalbond™-509 adhesive on glass rounds, oriented with the a-axis and c-axis parallel to the round. Orientation was determined visually using the distinct crystal morphology of olivine and clinopyroxene. Each olivine grain was ground and polished to create a surface intersecting their melt inclusions. The clinopyroxene grain was ground and polished to expose a large surface area while retaining as much thickness as possible. Grinding was accomplished with 600-grit silicon carbide sandpaper, while a series of diamond grits from 15 to 1 µm were used for final polishing. Polished grains had their adhesive dissolved in acetone and were re-adhered to the glass round with the grain's polished face down. The grains underwent an identical second stage of polishing to expose a second surface parallel to the first (Fig. 6). The same procedure was used: polishing until MI exposure for the olivines and to optimize area vs thickness for the clinopyroxene.

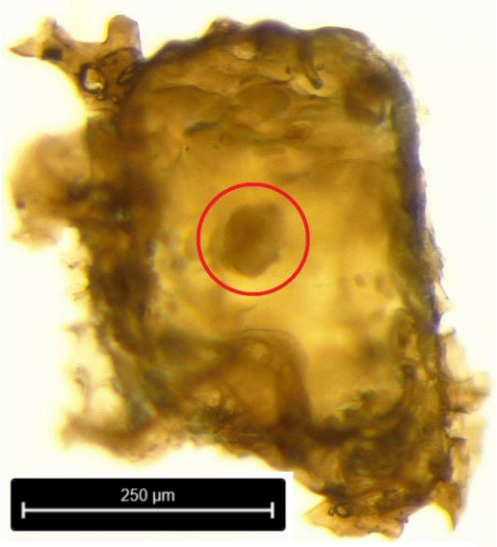

Fig. 5: Transmitted light photomicrograph of unpolished sample Ol-20, oriented normal to A-C crystallographic plane with the signature octagonal shape visible. Melt inclusion circled in red.

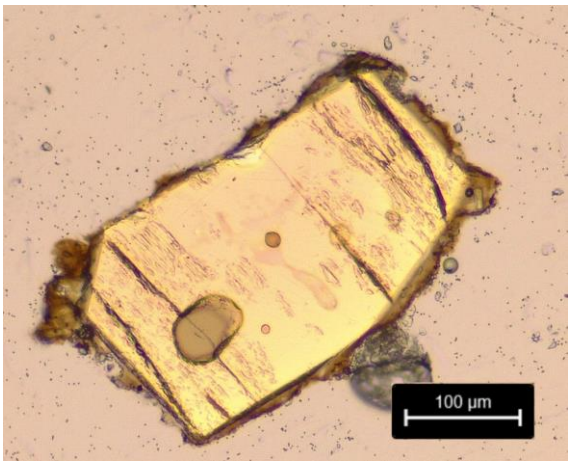

Fig. 6: Transmitted light photomicrograph of a doubly exposed melt inclusion (circled in red) in sample Ol-30. The grain is oriented normal to the A-C crystallographic plane.

4.2 Fourier-Transform Infrared Spectroscopy

The doubly polished olivine and clinopyroxene phenocrysts were analyzed using Fourier-transform infrared (FTIR) spectroscopy. FTIR spectroscopy functions by passing a changing polychromatic infrared beam, composed of multiple constituent wavelengths, through a sample and measuring the amount of IR radiation absorbed. Using the Fourier transform, the polychromatic beam is deconstructed back into discrete wavelengths — allowing multiple wavelengths to be measured simultaneously. Peaks in the resulting absorption spectrum correspond to vibrational frequencies of specific molecular bonding environments.

The adhesive mounting of each doubly polished grain was dissolved. The grains were then adhered to tape such that the melt inclusions included in olivine and the clinopyroxene's c-axis were exposed. The taped grains were transferred to a windowed sample slide for analysis. Three absorbance spectra were measured for each olivine

hosted MI. Absorbance spectra were measured every 30 µm along a 360 µm transect from the center to the rim of the clinopyroxene. The transect was measured parallel to the c-axis due to it being the axis of fastest diffusion in clinopyroxene. All measurements were performed using a Nicolet 6700 FT-IR Spectrometer at the Smithsonian Museum of Natural History's Department of Mineral Sciences.

Absorbance spectra were converted to water concentrations using the Beer-Lambert Law: $c = \frac{A}{\varepsilon l}$., where c is the concentration of the attenuating species A is absorbance, ε is the molar absorption coefficient of the attenuating species, and l is the optical path length (thickness). The height and area of fundamental water peaks (3350 to 3700 cm^{1}) for glass and mineral phases, respectively, were calculated using Pynams — an open-source python package for processing FTIR data (Ferriss, 2018). Spline baselines were employed to minimize the uncertainties associated with linear baselines. Thickness was determined by the proportional relationship with the number of interference fringes in regions of infrared reflectance (e.g. 2000 to 2700 cm^{-1}) (Fig. 7). Thickness was calculated to ± 3 µm with the equation $t = \frac{m}{2n(v_1 - v_2)}$, where t is the thickness (cm) of the sample, v_2 and v_1 are the minimum and maximum wavenumbers of the observed interval, m is the number of interference fringes occurring over the interval, and n is the sample's refractive index (Nichols and Wysoczanski, 2007). Molar H_2O absorption coefficients of 63 ± 5 $l \cdot mol^{-1} \cdot cm^{-1}$ for basaltic glass (Dixon et al., 1988), 34.515 ± 7.050 $l \cdot mol^{-1} \cdot cm^{-2}$ for olivine, and 46.103 ± 5.3 $l \cdot mol^{-1} \cdot cm^{-2}$ for clinopyroxene (Aubaud et al., 2009) were used.

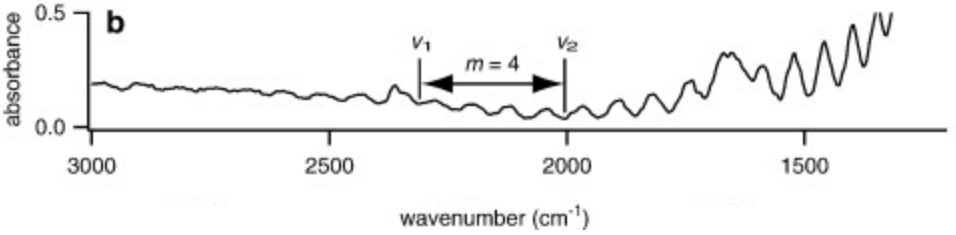

Fig. 7: Conceptual illustration of fringing, adapted from Nicholas and Wysoczanski, 2007. Fringes manifest as a series of peaks and valleys within an FTIR spectrograph most prominently between the wavenumbers of 2000 and 2700 for olivine.

4.3 Modeling Water Diffusion Rates

Time dependent 1D water diffusion gradients for the clinopyroxene were modeled in MATLAB as a function of the diffusion coefficient (D) of water in clinopyroxene and the partition coefficient of water between clinopyroxene and silicate melt (k_d). The strongly anisotropic water diffusion rates in clinopyroxene allows 1D diffusion models to provide results indistinguishable from 3D models (Thoraval and Demouchy, 2014). The Monte Carlo method was used to evaluate model uncertainties.

The composition of the clinopyroxene was constrained using rhyolite-MELTS, a thermodynamic model of phase equilibria in magmas (Gualda et al., 2012; Ghiorso and Gualda, 2015). An oxygen fugacity of 1 on the fayalite-magnetite-quartz (FMQ) scale was assumed representative of Mt. Pavlof for the rhyolite-MELTS calculations. This value was based on the FMQ of Mt. Emmons, an adjacent volcano within the same volcanic complex as Mt. Pavlof (Zimmer et al., 2010). The starting composition for the rhyolite-MELTS calculations was set to the composition of the bulk ash, as measured by inductively coupled plasma emission spectrometry in Terry Plank's laboratory at the Lamont-Doherty Earth Observatory. The partition coefficient was determined using the equation $\ln(k_d) = -4.2(\pm 0.2) + 6.5(\pm 0.5)X_{Al}^{Cpx} - 1(\pm 0.2)X_{Ca}^{Cpx}$, where X_j^{Cpx} is the fraction of cation *i* in the clinopyroxene on a six oxygen basis (O'Leary et al., 2010). The diffusion coefficient of water was determined to be between -9.0 and -10.0 $\log_{10}(m^2/s)$ based on similarities in iron and aluminum concentrations of the Pavlof clinopyroxene (based on our rhyolite-MELTS calculations) and clinopyroxene from the 1974 eruption of Volcan de Fuego (Ferriss et al., 2016). A degassing path was calculated using VolatileCalc 2.0, an excel based program for calculating H_2O-CO_2-Melt equilibrium for magmatic systems (Newman, 2002), with a starting H_2O concentration corresponding to the highest measured H_2O in the olivine-hosted melt inclusions. Selecting the highest H_2O melt inclusion to define the degassing path minimizes the effects of post-entrapment diffusive water loss from the inclusions (Lloyd et al. 2012).

5. Results

5.1 Melt Inclusion Analysis

Melt inclusions within olivines Ol-1, Ol-20, and Ol-21 underwent FTIR analysis of their hosted melt inclusions. Three spectrographs from each olivine-hosted melt inclusion were sampled using 256 counts with a 25 μm^2 aperture. Mean peak absorbance heights were measured at the principal water wavenumbers in silicate glass: 3350-3650 cm^{-1}. Peak height standard deviation was calculated using the equation $\sigma = \sqrt{\frac{\Sigma(x-\bar{x})^2}{(n-1)}}$,where *x* is the individual peak absorbance, $\bar{x}$ is the mean peak absorbance value, and *n* is the sample size. Thicknesses were determined by fringe counting within the 2000 to 2700 cm^{-1} wavenumber range (Fig. 7) using a refractive index of 1.546 (Nichols and Wysoczanski, 2007). Wt% H_2O was calculated with the Beer-Lambert Law ($c = \frac{A}{\varepsilon l}$) using the mean peak absorbance, the fringe calculated thickness, and a molar absorption coefficient of 63 ± 5 $l \cdot mol^{-1} \cdot cm^{-1}$ (Dixon and Delaney, 1988). Wt% H_2O uncertainties were evaluated using 1000-iteration Monte Carlo simulations — varying absorbance, thickness, density, and absorption coefficients within their respective uncertainties.

Sample	Mean Peak Absorbance	Absorbance σ	MI Thickness (μm)	Wt% H_2O	Wt% H_2O Uncertainty
Ol-1	0.872	0.073	44.2	1.92	0.29
Ol-20	0.382	0.056	32.9	1.13	0.23
Ol-21	0.595	0.078	23.5	2.50	0.55

Table 1: Absorbance, thickness, and Wt% values for samples Ol-1, Ol-20, and Ol-21. Standard deviations and uncertainties are of a 1-sigma, 65% confidence interval based on three sets 256-count analyses.

5.3 Clinopyroxene Water Diffusion

FTIR analysis was performed on a 360 μm center-to-edge transect along the c-axis of the sample Cpx-1. Thirteen points were measured to construct the transect; 512 counts were performed with an 80 by 20 μm aperture every 30 μm. The integrated area between the absorbance spectra of the principal water peaks, 3350-3650 cm^{-1} (Fig. 8), was calculated with spline baselines using Pynams (Ferriss, 2018). Water concentrations were between 14.8 to 64.9 ppm H_2O from the edge to the center of the crystal.

1D diffusive water loss was modeled for the clinopyroxene along a VolatileCalc 2.0 calculated degassing path resulting in an initial pressure of 130.8 MPa, equivalent to a depth of approximately 2.4 km. Diffusion parameters, including normally distributed 2-sigma uncertainties, were -3.91 ± 0.281 ln(k_d) and a diffusion coefficient of -9.5 ± 0.5 $\log_{10}(m^2/s)$. Uncertainties were evaluated by a 2000-iteration Monte Carlo analysis (Fig. 9). The 1D model resulted in an ascent rate of -1.02 ± 0.872 $\log_{10}$(MPa/S) (2-sigma), equivalent to a mean ascent rate of 0.097 MPa/S.

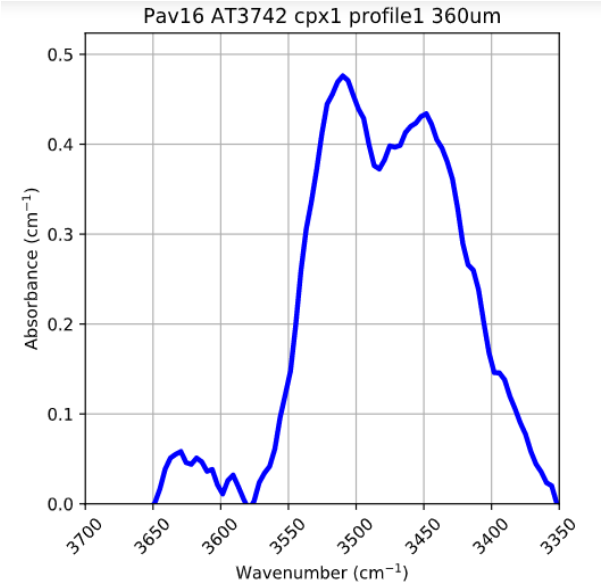

Fig. 8: The baseline corrected absorption spectra at the center of Cpx-1 in Pynams, zoomed in to emphasis H_2O absorbance peaks.

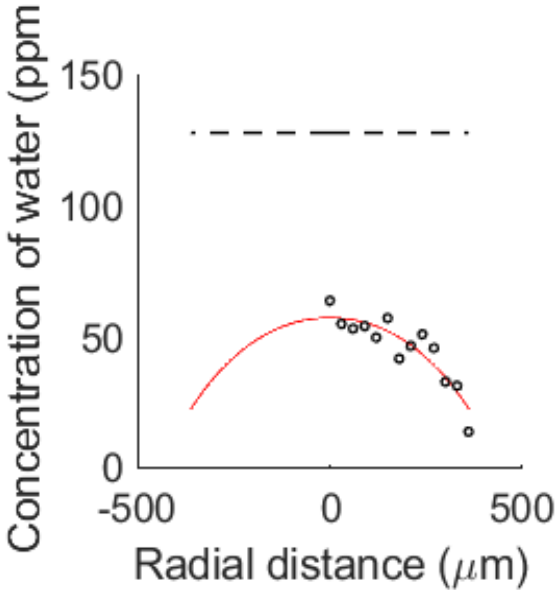

Fig. 9: Example modeled diffusion curve. Circles are H_2O measurements, dashed black line is the initial H_2O, red line is a least-squares fitted diffusion product.

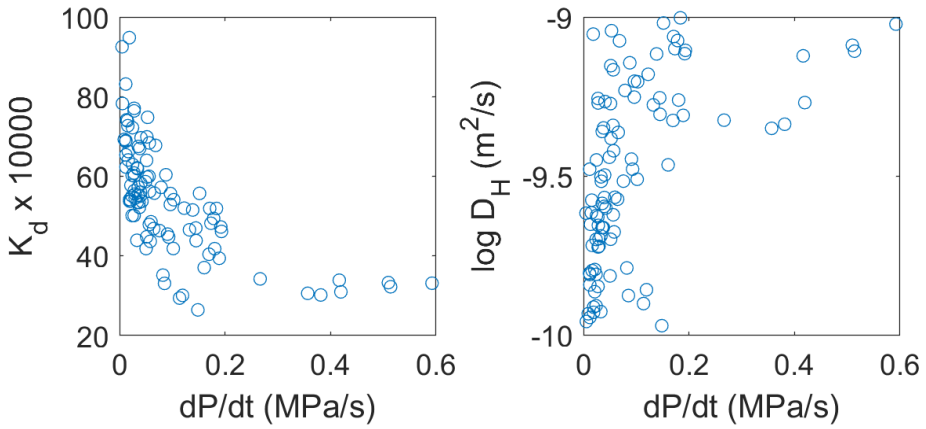

Fig. 10: A 100-iteration subset of solutions generated by Monte Carlo analysis: partition coefficient vs ascent rate (left) and diffusion vs. ascent rate (right).

6. Discussion

Our results support the hypothesis that the syneruptive magma ascent rate during Mount Pavlof's 2016 eruption is outside the uncertainty of comparable low VEI eruptions. A limited set of water diffusion chronometry studies utilizing either melt inclusions or melt embayments have been conducted on VEI 1-4 eruptions (Fig. 11) (Table 2). Pavlof's 2016 magma ascent rate of -1.02 ± 0.872 $\log_{10}$(MPa/s) falls beyond the 95-percent confidence interval for magma ascent rates during Cerro Negro's explosive eruptions in 1992 and 1995 — classified as VEI 3 and 2 respectively (Barth et al., 2019). At -1.30 ± 0.05 $\log_{10}$(MPa/s), the ascent rate for Kilauea Iki's 1959 VEI 2 eruption is firmly within Pavlof's uncertainty. However, Kilaeuea Iki's eruption was a low viscosity fire fountain. This fundamentally different style of eruption is not necessarily reflective of the plumbing and ascent conditions during typical explosive basalt eruptions such as those at Pavlof and Cerro Negro (Ferguson et al., 2016). At the upper limits, Pavlof's 2016 ascent rate overlaps with Vulcán de Fuego's 1974 VEI 4 eruption.

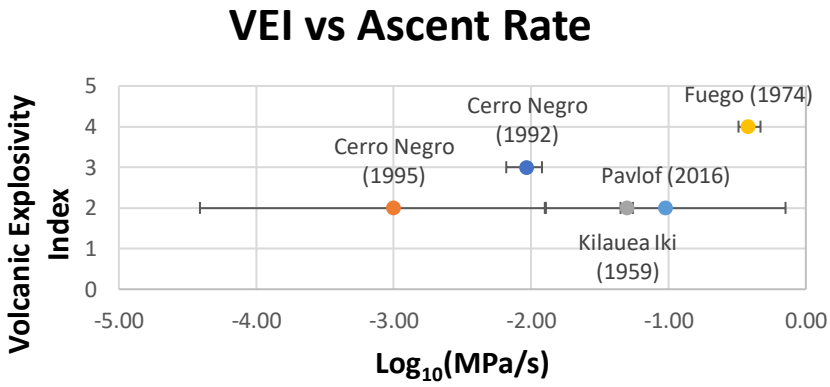

Fig. 11: VEI vs Log_{10}(MPa/s). Ascent rates determined using melt inclusions at Cerro Negro (Barth et al., 2019) and Mount Pavlof (this study). Vulcán de Fuego (Lloyd et al., 2014) and Kilauea Iki (Ferguson et al., 2016) were determined with melt embayments.

Eruption	VEI	Median Log_{10}(MPa/s))	Min (Log_{10}(MPa/s))	Max Log_{10}(MPa/s)
Kiluaea Iki (1959)	2	-1.15	-1.70	-0.89
Cerro Negro (1995)	2	-3.0	-4.41	-1.90
Cerro Negro (1992)	3	-2.03	-2.18	-1.92
Fuego (1974)	4	-1.30	-1.35	-1.26

Table 2: Log_{10}(MPa/s) distribution and VEI for Cerro Negro, Kiluaea Iki, and Fuego eruptions. Ascent rats determined using melt inclusions at Cerro Negro (Barth et al., 2019). Vulcán de Fuego (Lloyd et al., 2014) and Kilauea Iki (Ferguson et al., 2016) were determined with melt embayments.

The relationship between plume height and mass eruption rate (MER) offers further evidence for a greater eruptive intensity during Pavlof's 2016 eruption, in addition to secondary validation of model results. Conservation of mass relates MER (Q) in kg/s to density (q) in kg/m^3, conduit cross-sectional area (A) in m^2, and magma ascent rate (u) in m/s by the equation $Q = quA$ (Barth et al., 2019). Observational evidence relates maximum plume height (H) and volumetric flow rate through the equation $H = 2.00(uA)^{0.241}$ (Mastin et al., 2009). Applying these equations to Pavlof's 2016 eruption, using a conduit radius of 10 m (Fee et al., 2017) and q of 2500 kg/m^3 for water saturated crystal laden melts (Mastin et al., 2009), and the diffusion-modeled ascent rate yields a mass eruption rate of 6.4 ± 0.2 log_{10}(kg/s) and maximum plume height of 11.2 ± 2.7 km (1-sigma uncertainties). The predicted plume height agrees with observations, validating the diffusion-modeled ascent rate. The observed and calculated plume heights for Mount Pavlof follow the same trend as ascent rate; Pavlof's plume exceeds Cerro Negro's 1992 and 1995 eruptions' plume heights and MER while being overshadowed by those of Fuego's 1974 eruption (Table 3).

Eruption	VEI	Mass Eruption Rate Log_{10}(kg/s)	Plume Height (km)
Pavlof (2016)	2	6.4	9
Kiluaea Iki (1959)	2	5.9	0.4
Cerro Negro (1995)	2	4.1	3
Cerro Negro (1992)	3	5.0	7
Fuego (1974)	4	6.5	15

Table 3: VEI in comparison to mass eruption rate and observed plume heights. Kiluaea Iki, Cerro Negro, and Fuego MERs are adapted from Barth et al. (2019): Fig. 14. Plume heights are from Barth et al. (2009) — Cerro Negro; Ferguson et al. (2016) — Kilauea Iki; Lloyd et al. (2014) — Fuego. Kiluaea Iki's plume height is not representative of typical basaltic eruptions.

7. Conclusion

Water diffusion chronometry of olivine and clinopyroxene from 2016 eruption of Mount Pavlof indicate an exceptional ascent rate of 0.097 MPa/s — faster than previous diffusion-based rates for explosive VEI 2 and 3 eruptions. Plume height observations and

calculated mass eruption rates corroborate an atypical ascent rate for a VEI 2 eruption, with the 9 km plume indicative of VEI 3 eruptions (Newhall and Self, 1986). Comparison to prior research is limited in large part by a small, localized sample which may bias data towards a single phase of the eruption, highlighting the need for time-stamped samples throughout the total eruption duration. An increase in the number of analyzed grains and direct measurement of water diffusion coefficients through sub-solidus heating of the samples would further refine uncertainties (Ferriss et al., 2016). Narrowing uncertainty in the ascent rate could further distinguish the 2016 Pavlof eruption from other low VEI eruptions and that of Vulcán de Fuego's 1974 eruption — offering greater insight into the variety of spatially and temporally distant volcanic systems.

8. Bibliography

Aubaud, C., Bureau, H., Raepsaet, C., Khodja, H., Withers, A. C., Hirschmann, M. M., & Bell, D. R. (2009). Calibration of the Infrared Molar Absorption Coefficients for H in Olivine, Clinopyroxene and Rhyolitic Glass by Elastic Recoil Detection Analysis. Chemical Geology, 262(1-2), 78–86.

Barth, A., Newcombe, M., Plank, T., Gonnermann, H., Hajimirza, S., Soto, G. J., Hauri, E. (2019). Magma decompression rate correlates with explosivity at basaltic volcanoes — Constraints from water diffusion in olivine. Journal of Volcanology and Geothermal Research, 387.

Chen, Y., Provost, A., Schiano, P., & Cluzel, N. (2013). Magma ascent rate and initial water concentration inferred from diffusive water loss from olivine-hosted melt inclusions. Contributions to Mineralogy and Petrology, 165(3), 525–541.

Dixon, J. E., Stolper, E., & Delaney, J. R. (1988). Infrared spectroscopic measurements of CO2 and H2O in Juan de Fuca Ridge basaltic glasses. Earth and Planetary Science Letters, 90(1), 87–104.

Fee, D., Haney, M. M., Matoza, R. S., Eaton, A. R. V., Cervelli, P., Schneider, D. J., & Iezzi, A. M. (2017). Volcanic tremor and plume height hysteresis from Pavlof Volcano, Alaska. Science, 355(6320), 45–48.

Ferguson, D. J., Gonnermann, H. M., Ruprecht, P., Plank, T., Hauri, E. H., Houghton, B. F., & Swanson, D. A. (2016). Magma decompression rates during explosive eruptions of Kīlauea volcano, Hawaii, recorded by melt embayments. Bulletin of Volcanology, 78(10).

Ferriss, E. (2018) Pynams: a Python package for interpreting FTIR spectra of nominally anhydrous minerals (NAMs), v0.2.0; Zenodo.

Ferriss, E., Plank, T., Newcombe, M., Walker, D., & Hauri, E. (2018). Rates of dehydration of olivines from San Carlos and Kilauea Iki. Geochimica et Cosmochimica Acta, 242, 165–190.

Ferriss, E., Plank, T., & Walker, D. (2016). Site-specific hydrogen diffusion rates during clinopyroxene dehydration. Contributions to Mineralogy and Petrology, 171(6).

Ghiorso M.S., Gualda, G.A.R., (2015) An H2O-CO2 mixed fluid saturation model compatible with rhyolite-MELTS. Contributions to Mineralogy and Petrology, 169(53).

Gonnermann, H. M., & Manga, M. (2012). “Dynamics of Magma Ascent in the Volcanic Conduit.” Modeling Volcanic Processes: The Physics and Mathematics of Volcanism, 55–84.

Gualda G.A.R., Ghiorso M.S., Lemons R.V., Carley T.L. (2012) Rhyolite-MELTS: A modified calibration of MELTS optimized for silica-rich, fluid-bearing magmatic systems. Journal of Petrology, 53, 875-890.

Larsen, J. F. (2016). Unraveling the diversity in arc volcanic eruption styles: Examples from the Aleutian volcanic arc, Alaska. Journal of Volcanology and Geothermal Research, 327, 643–668.

Lloyd, A. S., Plank, T., Ruprecht, P., Hauri, E. H., & Rose, W. (2012). Volatile loss from melt inclusions in pyroclasts of differing sizes. Contributions to Mineralogy and Petrology, 165(1), 129–153.

Lloyd, A. S., Ruprecht, P., Hauri, E. H., Rose, W., Gonnermann, H. M., & Plank, T. (2014). NanoSIMS results from olivine-hosted melt embayments: Magma ascent rate during explosive basaltic eruptions. Journal of Volcanology and Geothermal Research, 283, 1–18.

Lloyd, A. S., Ferriss, E., Ruprecht, P., Hauri, E. H., Jicha, B. R., & Plank, T. (2016). An Assessment of Clinopyroxene as a Recorder of Magmatic Water and Magma Ascent Rate. Journal of Petrology, 57(10), 1865–1886.

Loughlin, S.C., Vye-Brown, C., Sparks, R.S.J. and Brown, S.K. et al. (2015) Global volcanic hazards and risk: Summary background paper for the Global Assessment Report on Disaster Risk Reduction 2015. Global Volcano Model and IAVCEI.

Mangan, M., Miller, T., Waythomas, C., Trusdell, F., Calvert, A., & Layer, P. (2009). Diverse lavas from closely spaced volcanoes drawing from a common parent: Emmons Lake Volcanic Center, Eastern Aleutian Arc. Earth and Planetary Science Letters, 287(3-4), 363–372.

Mastin, L., Guffanti, M., Servranckx, R., Webley, P., Barsotti, S., Dean, K., … Waythomas, C. (2009). A multidisciplinary effort to assign realistic source parameters to models of volcanic ash-cloud transport and dispersion during eruptions. Journal of Volcanology and Geothermal Research, 186(1-2), 10–21.

Newhall, C. G., & Self, S. (1986). The Volcanic Explosivity Index (VEI): An estimate of explosive magnitude for historical volcanism. History of Geophysics History of Geophysics: Volume 2, 143–150.

Newman, S., & Lowenstern, J.B. (2002). VolatileCalc: a silicate melt-H2O-CO2 solution model written in Visual Basic for Excel. Computers and Geosciences, 28(5), 597-604.

Nichols, A. R. L., & Wysoczanski, R. J. (2007). Using micro-FTIR spectroscopy to measure volatile contents in small and unexposed inclusions hosted in olivine crystals. Chemical Geology, 242(3-4), 371–384.

O'leary, J. A., Gaetani, G. A., & Hauri, E. H. (2010). The effect of tetrahedral Al3 on the partitioning of water between clinopyroxene and silicate melt. Earth and Planetary Science Letters, 297(1-2), 111–120.

Thoraval, C., & Demouchy, S. (2014). Numerical models of ionic diffusion in one and three dimensions: application to dehydration of mantle olivine. Physics and Chemistry of Minerals, 41(9), 709–723.

Toramaru, A. (1989). Vesiculation process and bubble size distributions in ascending magmas with constant velocities. Journal of Geophysical Research, 94(B12), 17523–17542.

Weis, F. A., Lazor, P., & Skogby, H. (2018). Hydrogen analysis in nominally anhydrous minerals by transmission Raman spectroscopy. Physics and Chemistry of Minerals, 45(7), 597–607.

Woods, S. C., Mackwell, S., & Dyar, D. (2000). Hydrogen in diopside: Diffusion profiles. American Mineralogist, 85(3-4), 480–487.

Zhang, Y., Xu, Z., Zhu, M., & Wang, H. (2007). Silicate melt properties and volcanic eruptions. Reviews of Geophysics, 45(4).

Zimmer, M. M., Plank, T., Hauri, E. H., Yogodzinski, G. M., Stelling, P., Larsen, J., … Nye, C. J. (2010). The Role of Water in Generating the Calc-alkaline Trend: New Volatile Data for Aleutian Magmas and a New Tholeiitic Index. Journal of Petrology, 51(12), 2411–2444.

9. Appendix

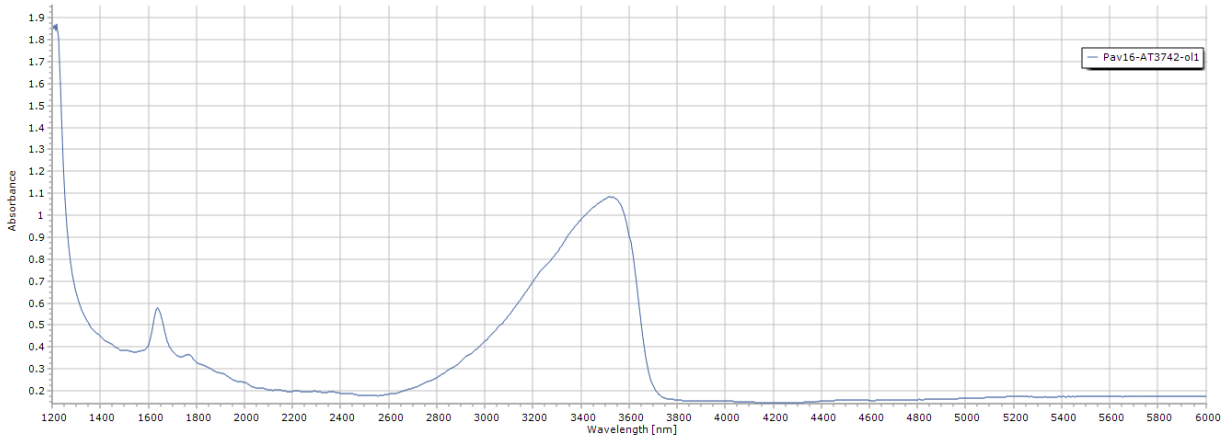

Supplementary Fig. 1: Example raw FTIR absorbance spectra of Ol-1.

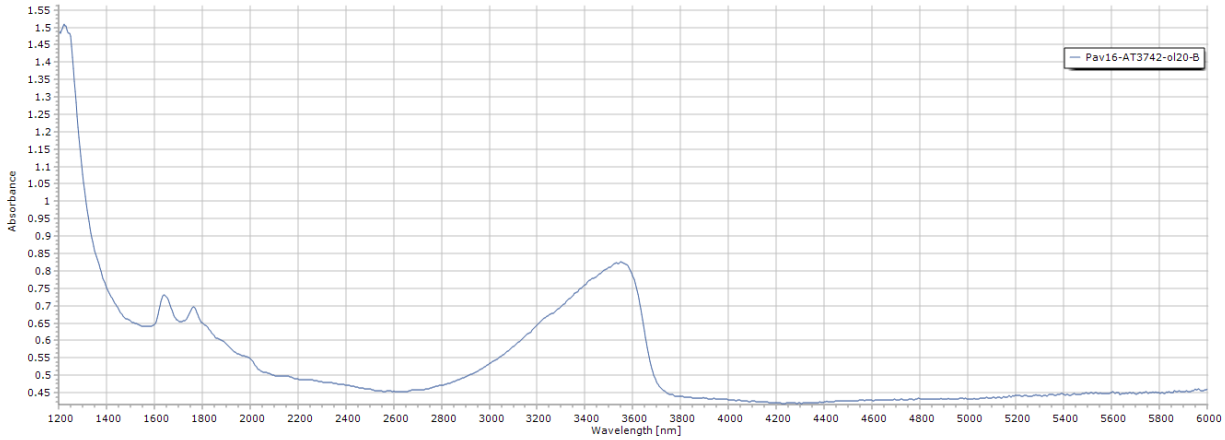

Supplementary Fig. 2: Example raw FTIR absorbance spectra of Ol-20.

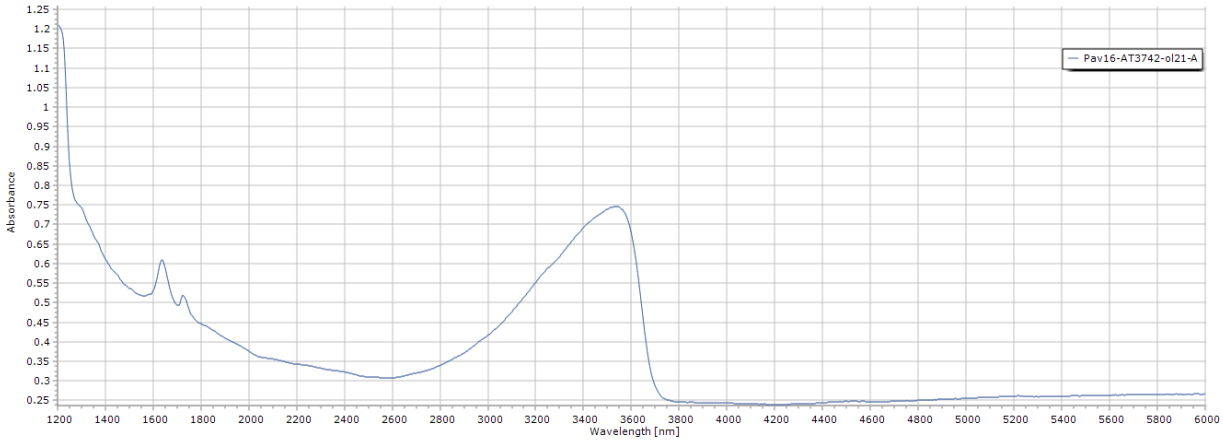

Supplementary Fig. 3: Example raw FTIR absorbance spectra of Ol-21.

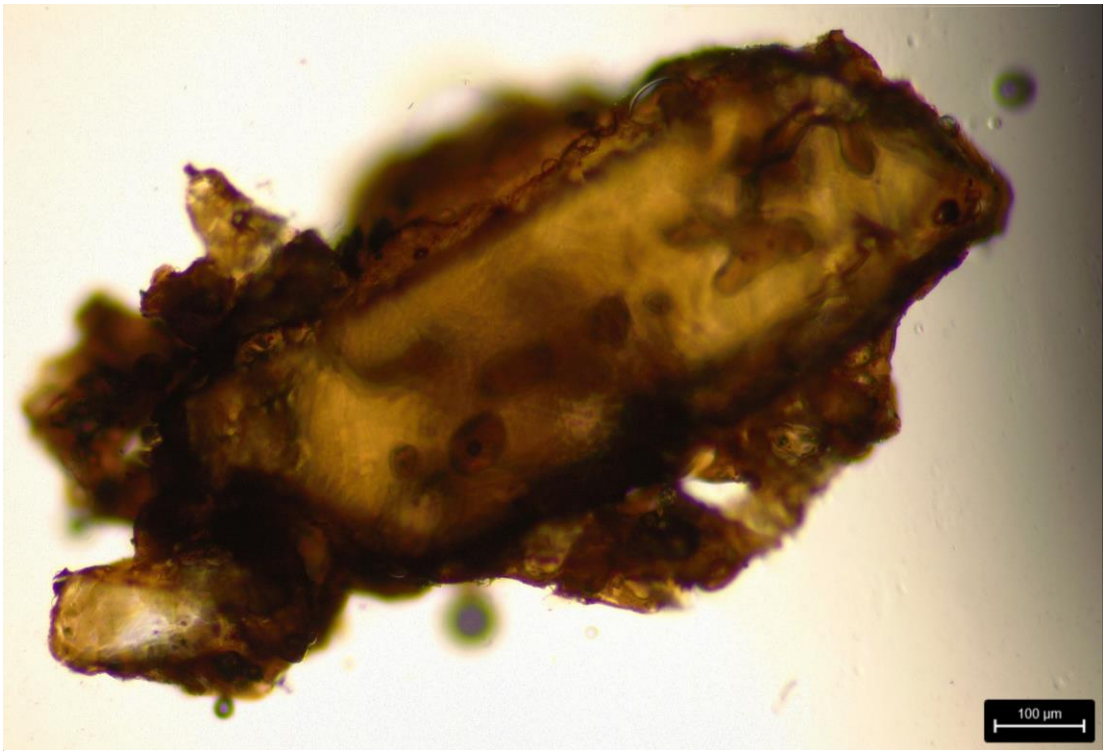

Supplementary Fig. 4: Transmitted light microphotograph of unpolished Ol-1, 200x magnification.

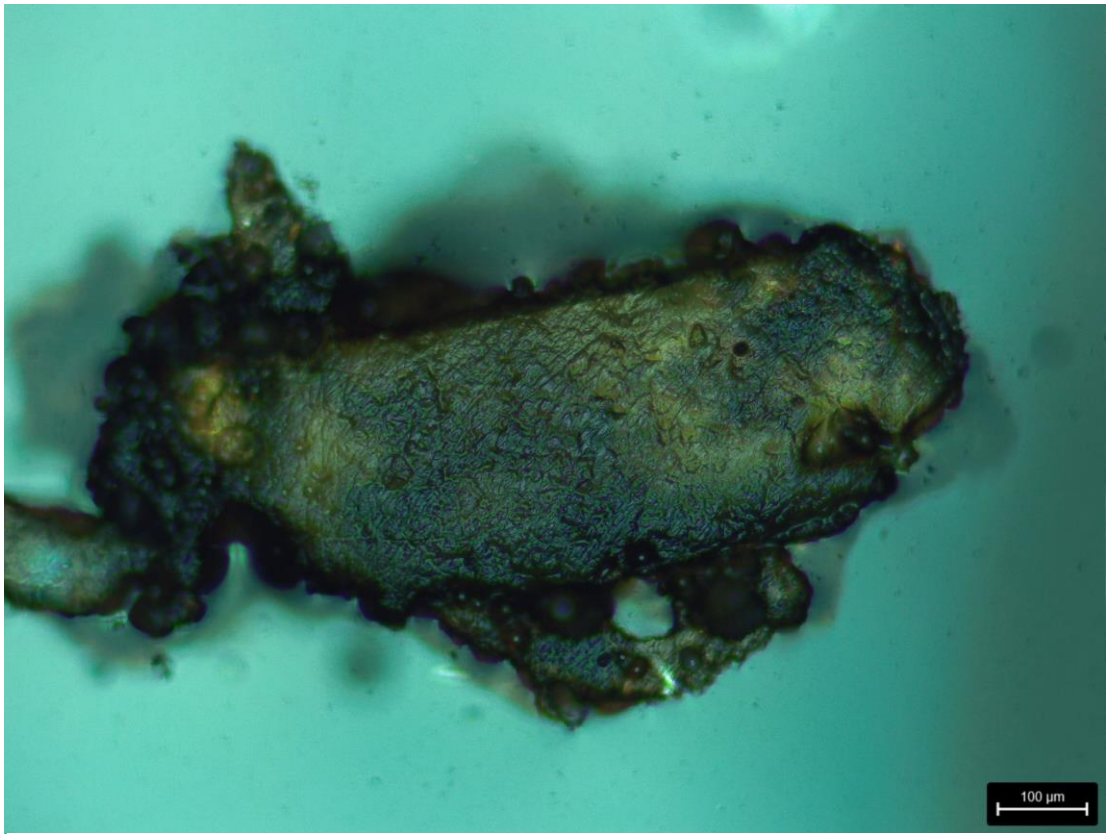

Supplementary Fig. 5: Reflected light microphotograph of ongoing polishing of Ol-1, 200x magnification.

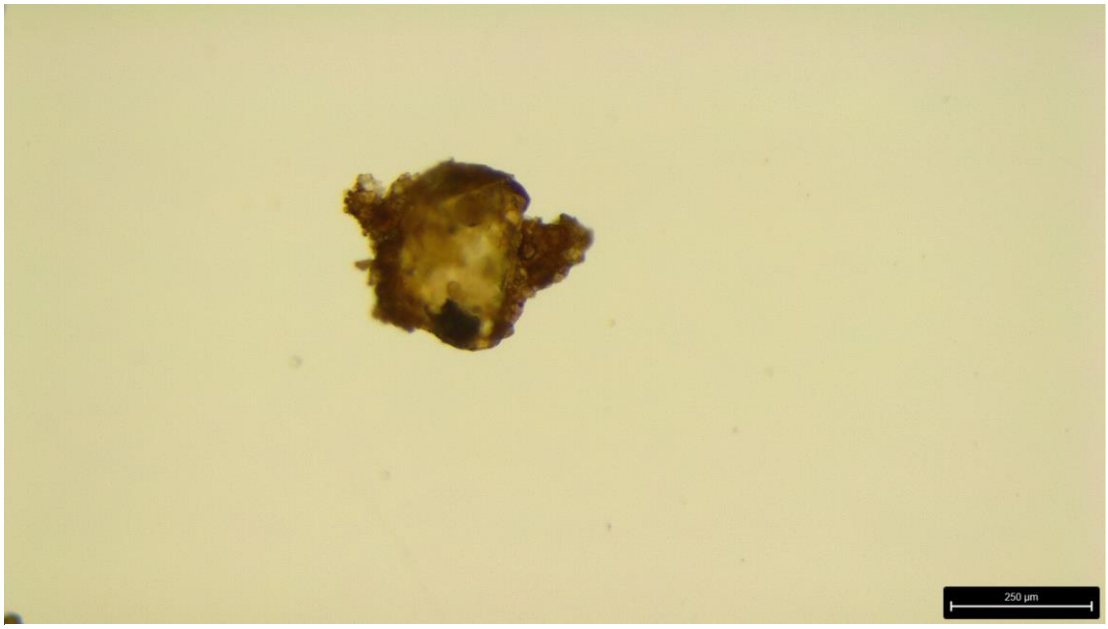

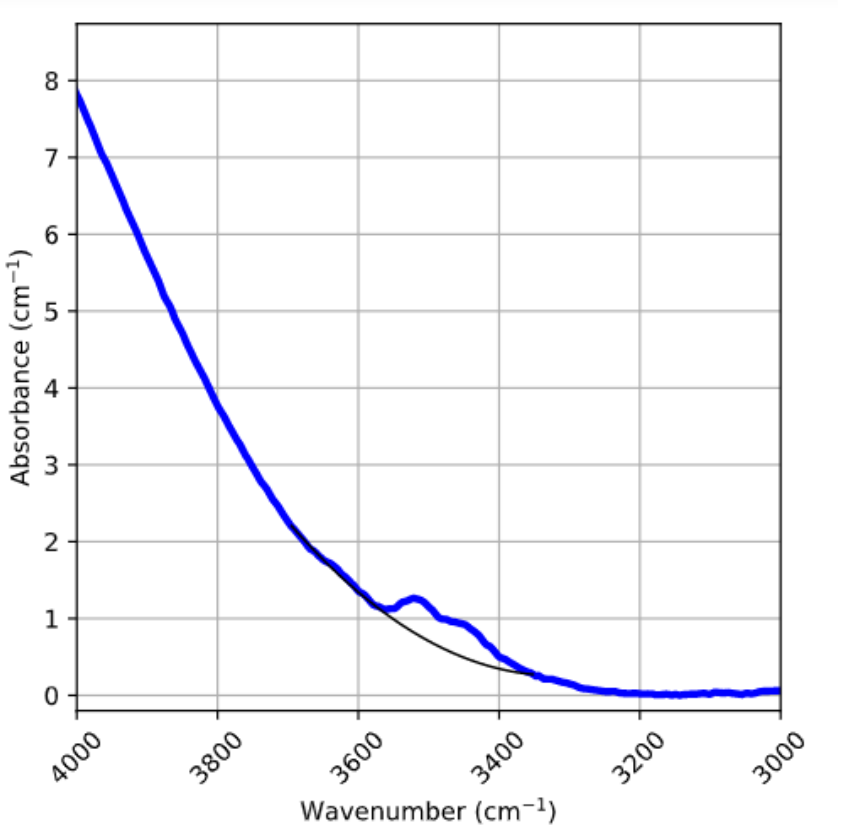

Supplementary Fig. 7: Non baseline-corrected absorbance spectra of Cpx-1, zoomed in on H_2O peaks (Ferriss, 2018).

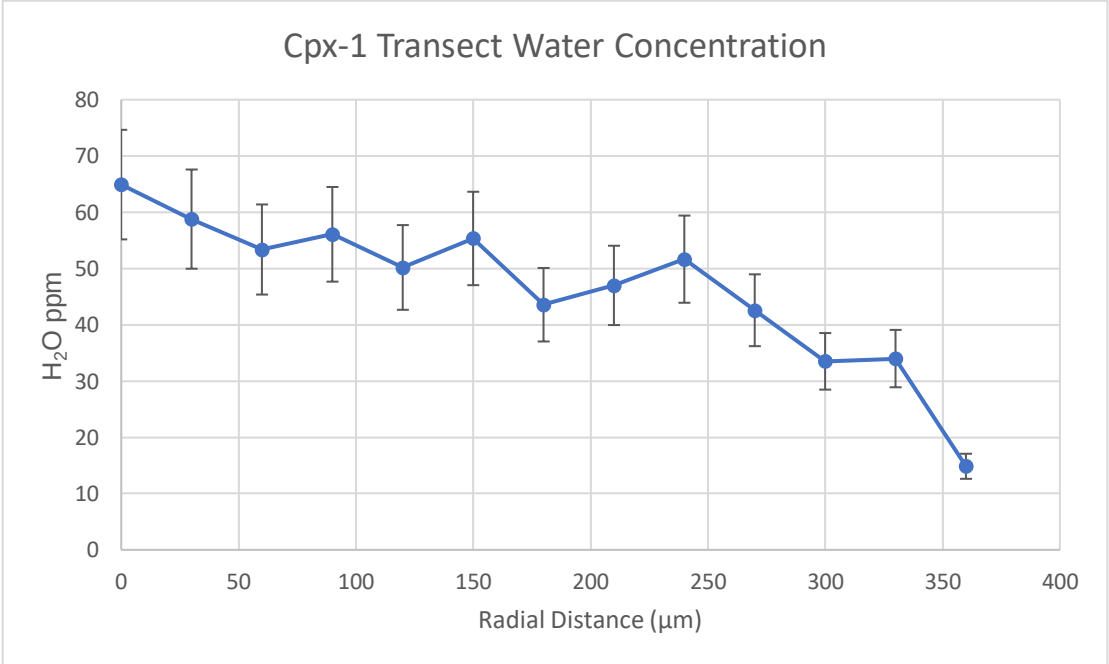

Supplementary Fig. 8: Measured water gradient in Cpx-1, parallel to crystallographic c-axis.

I pledge on my honor that I have not given or received any unauthorized assistance on this assignment.

Nicholas Alan Culbreth